Volume 1 | Number 1 | Jan 2013 | Pages 1–100

PCCP

Physical Chemistry Chemical Physics
www.rsc.org/pccp

ROYAL SOCIETY OF CHEMISTRY

This is an *Accepted Manuscript*, which has been through the Royal Society of Chemistry peer review process and has been accepted for publication.

Accepted Manuscripts are published online shortly after acceptance, before technical editing, formatting and proof reading. Using this free service, authors can make their results available to the community, in citable form, before we publish the edited article. We will replace this *Accepted Manuscript* with the edited and formatted *Advance Article* as soon as it is available.

You can find more information about *Accepted Manuscripts* in the **Information for Authors**.

Please note that technical editing may introduce minor changes to the text and/or graphics, which may alter content. The journal's standard **Terms & Conditions** and the **Ethical guidelines** still apply. In no event shall the Royal Society of Chemistry be held responsible for any errors or omissions in this *Accepted Manuscript* or any consequences arising from the use of any information it contains.

High Thermoelectric Performance from Optimization of Hole-Doped CuInTe$_2$

Gang Zhou and Dong Wang[*]

MOE Key Laboratory of Organic OptoElectronics and Molecular Engineering,

Department of Chemistry, Tsinghua University, Beijing, 100084, People's Republic of

China

[*]Corresponding author email: dong913@tsinghua.edu.cn

Phone: +86-10-62798081

Postal address: Department of Chemistry, Tsinghua University, Beijing, 100084,

People's Republic of China

Abstract

We investigated the electronic structure, lattice dynamics and thermoelectric transport properties of $CuInTe_2$ based on first-principles calculations. From the analysis of density of states and partial charge density, it can be expected that p-doping at the In-site or n-doping at the Cu-site will barely modify the electronic states near the valence or conduction band edge but increase the carrier concentration to achieve the highest thermoelectric efficiency. Lattice dynamics calculations suggest that the thermal conductivity of $CuInTe_2$ can be effectively reduced by introducing structural defects at Cu, In and Te sites. The p-type $CuInTe_2$ possesses better thermoelectric properties as compared to the n-type one, which mainly originates from the steeper density of states resulting from nearly degenerate valence bands near the band edge. The temperature dependence of the thermoelectric transport properties of p-type $CuInTe_2$ at different carrier concentrations was studied in detail, which is found to be in good agreement with the experimental data. Our results of calculation showed that p-type $CuInTe_2$ can achieve an upper-limit figure of merit value of 1.72 at 850 K and are promising thermoelectric materials for waste heat recovery at medium temperatures.

I. Introduction

Under the challenges of global energy crisis and climate change, thermoelectric materials, which can be utilized to directly convert heat into electricity in the solid state, have gained renewed interests in recent years.[1-5] The energy conversion efficiencies of thermoelectric devices are characterized by the dimensionless thermoelectric figure of merit of materials:[1, 6] $ZT = S^2\sigma T\big/\kappa$, where S, σ, T and κ denote the Seebeck coefficient, electrical conductivity, temperature and thermal conductivity. Both electrons and phonons are heat carriers therefore the thermal conductivity can be decomposed into two independent contributions. As a result, there exist two major strategies to improve the thermoelectric efficiency: band structure engineering to optimize electrical properties[4, 6, 7] and phonon engineering to decrease the phonon thermal conductivity[1, 7, 8]. However, due to the interdependence of Seebeck coefficient, electrical conductivity and electronic thermal conductivity, it makes the maximization of ZT a challenge so far.[2, 3, 9]

Recently, a ternary compound CuInTe2 with pseudocubic structures has been reported to exhibit promising thermoelectric properties in moderate temperature range.[10-12] It was experimentally found that the ZT value of $CuInTe_2$ can reach 1.18 at 850 K.[11] Yang *et al.* have reported that the ZT value of $CuInTe_2$ can be effectively improved by simultaneous Zn substitution for both Cu and In, and they achieved a ZT value of 0.69 at 737 K, which is 1.65 times that of Zn-free CuInTe2.[13] Chen *et al.* have investigated the thermoelectric properties of CuInTe2/graphene composites and

obtained an improved *ZT* value due to the decreased thermal conductivity.[12] Impurity doping is an effective method to optimize the carrier concentration and improve the thermoelectric properties of materials.[14] First-principles electronic structure calculations can help us to identify the appropriate doping sites to optimize the carrier concentration whereas not to modify the electronic states of pristine materials. In this work, we have investigated thermoelectric transport properties of $CuInTe_2$ by using first-principles methods and Boltzmann transport equations. We analyzed how features in the band structure of $CuInTe_2$ affect the electrical transport properties, and identified the optimal doping sites and level to maximize the thermoelectric performance of $CuInTe_2$. Lattice dynamics analysis also help us to identify the proper sites to introduce the structural defects for further reduction of the lattice thermal conductivity. Our investigations established an upper bound of thermoelectric figure of merit for $CuInTe_2$ and demonstrated that an improvement over the previously reported values is possible under optimal conditions.

II. Computational methods

The energy band calculations have been performed by using the projector augmented wave (PAW) method within the framework of density functional theory as implemented in the Vienna *Ab initio* Simulation Package (VASP).[15-17] The generalized gradient approximation (GGA) in the Perdew-Burke-Ernzerh (PBE) functional form[18] was applied. The geometry for $CuInTe_2$ is fully relaxed until the magnitude of the force acting on all atoms is less than 0.01 eV/Å and the total energy converges

within 0.001 meV. The cutoff energy was set to be 500 eV for the plane-wave expansion and the Monkhorst-Pack **k-**mesh of $7 \times 7 \times 7$ was adopted for the integration of Brillouin zone. Being strongly localized, the exchange-correlation effects of the Cu 3d electrons are not adequately described within the generalized gradient approximation. This can be to some extent corrected with the DFT+U method, which is a combination of the DFT and Hubbard Hamiltonian for the Coulomb repulsion. Here we chose the PBE+U method to calculate the electronic structure of $CuInTe_2$. The effective Coulomb repulsion parameter U was set to be 4 eV according to the previously reported value of Cu-based ternary semiconductors.[19]

The phonon properties were derived from the lattice dynamics computations using the ab initio force constant method as implemented in the PHONOPY code.[20] Supercells were constructed as a $2 \times 2 \times 2$ tetragonal unit cell, corresponding to 8 unit cells in the tetragonal setting containing 128 atoms. Symmetry-inequivalent atomic displacements were generated to obtain forces from VASP and then phonon frequencies can be derived from second-order force constants, which were obtained by the finite-difference of forces.

On the basis of the electronic band structure, the thermoelectric transport properties can be evaluated by using the semi-classical Boltzmann transport equations with the relaxation time approximation, as implemented in the BoltzTraP code.[21] The thermoelectric transport coefficients σ, S and κ_e can be written in a compact form in terms of the $\Lambda^{(\alpha)}$ function [6, 22]

$$\sigma = \Lambda^{(0)} \ , \tag{1}$$

$$S = -\frac{1}{eT}\left(\frac{\Lambda^{(1)}}{\Lambda_{(0)}}\right), \tag{2}$$

$$\kappa_e = \frac{1}{e^2T}\left\{\Lambda^{(2)} - \frac{\left[\Lambda^{(1)}\right]^2}{\Lambda^{(0)}}\right\}, \tag{3}$$

where

$$\Lambda^{(\alpha)} = \int d\varepsilon\left(-\frac{\partial f_0}{\partial \varepsilon}\right)(\varepsilon - E_F)^\alpha \Sigma(\varepsilon) \ , \tag{4}$$

where e is the elementary charge of the carriers, T is the temperature, E_F is the Fermi level, f_0 is the Fermi-Dirac distribution function, and $\Sigma(\varepsilon)$ is the transport distribution function which can be expressed as

$$\Sigma(\varepsilon) = \frac{e^2}{N_{\mathbf{k}}\Omega}\sum_{i,\mathbf{k}}\mathbf{v}_{i,\mathbf{k}}\mathbf{v}_{i,\mathbf{k}}\tau_{i,\mathbf{k}}\delta(\varepsilon - \varepsilon_i(\mathbf{k})), \tag{5}$$

where i and $\mathbf{k}$ are the band index and wave vector, respectively, and $\tau_{i,\mathbf{k}}$ is the relaxation time, $N_{\mathbf{k}}$ is the number of the sampled $\mathbf{k}$ points in the Brillouin zone (BZ), and Ω is the volume of unit cell, $\mathbf{v}_{i,\mathbf{k}}$ is the group velocity of the carriers in the band i with wave vector $\mathbf{k}$. The velocity $\mathbf{v}_{i,\mathbf{k}}$ can be determined from a $\mathbf{k}$-space gradient

$$\mathbf{v}_{\mathbf{k}} = \frac{1}{\hbar}\frac{\partial \varepsilon_i(\mathbf{k})}{\partial \mathbf{k}}, \tag{6}$$

which requires the eigenvalues on a dense $\mathbf{k}$ mesh for an accurate evaluation.
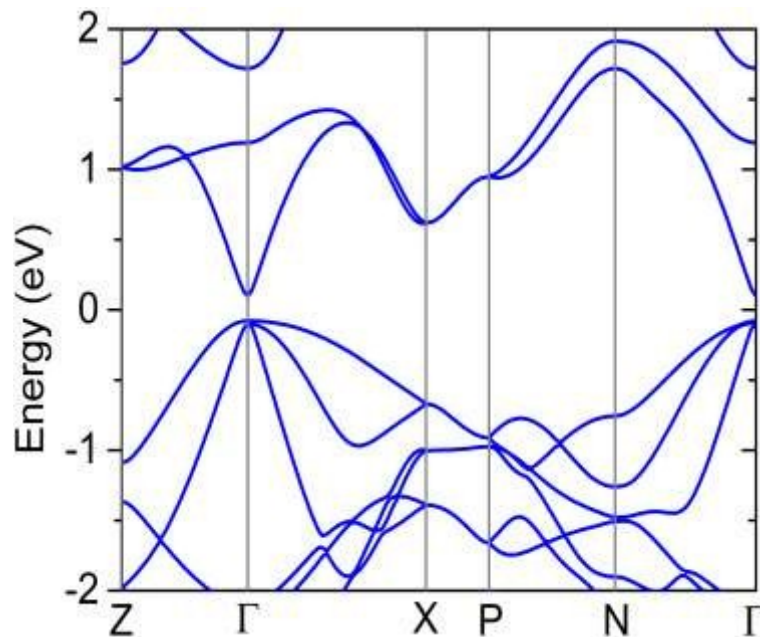
III. Results and discussion

Figure 1. Band structures of CuInTe$_2$.

CuInTe$_2$ is crystallized in tetragonal structure with a space group of I-42d, which may be derived from the diamond-like cubic zinc-blende material.[12] Fig. 1 shows the *ab initio* electronic band structure of CuInTe$_2$. Our results of calculation show that the fundamental gap of CuInTe$_2$ is direct at Γ-point in the BZ with a magnitude of 0.177 eV (see Fig. 1). In contrast to the zinc blende lattice, the triply degenerate valence band Γ_{15v} in CuInTe$_2$ splits into a non-degenerate band Γ_{4v} and a doubly degenerate band Γ_{5v} due to the crystal field effect.[10] The tetragonal distortion parameter η (= $c/2a$) of CuInTe$_2$ is very close to 1, which causes a small crystal field splitting energy.[10]   Therefore, the valence bands at Γ point are nearly triply degenerate. The non-degenerate band Γ_{4v} is light-hole band while doubly degenerate band Γ_{5v} is heavy-hole band. Such a mixture of heavy and light bands near the valence band maximum (VBM) that are nearly degenerate indicates a promising

7

thermoelectric performance for p-type doping.[23, 24] In comparison with previous calculations,[23] our calculated crystal field splitting energy is significantly smaller. The conduction bands exhibit a strong dispersion near the band edge and then become relatively flat with the increasing energy. The calculated band gap is smaller than the experimentally measured gap,[12] which originates from the fact that standard density functional theory usually underestimates the band gaps of semiconductors. In order to achieve a better agreement between theory and experiment, the band gap of $CuInTe_2$ was adjusted to match the experimental data by applying the so-called scissor operator in our subsequent calculations of transport properties. Similar treatments have been widely adopted in previous calculations.[25, 26] The scissor operator does not change the band dispersion and group velocities, so the only influence of band gap adjustment is on the carrier concentration dependence of Seebeck coefficients. When the Fermi level is in the gap and the carrier concentration is low, both conduction and valence bands may contribute to the Seebeck coefficients with opposite signs, resulting in a drop of the Seebeck coefficients at low carrier concentrations. This is known as the bipolar effect. Without the band gap adjustment, the bipolar effect will be more pronounced since the band gap is underestimated.
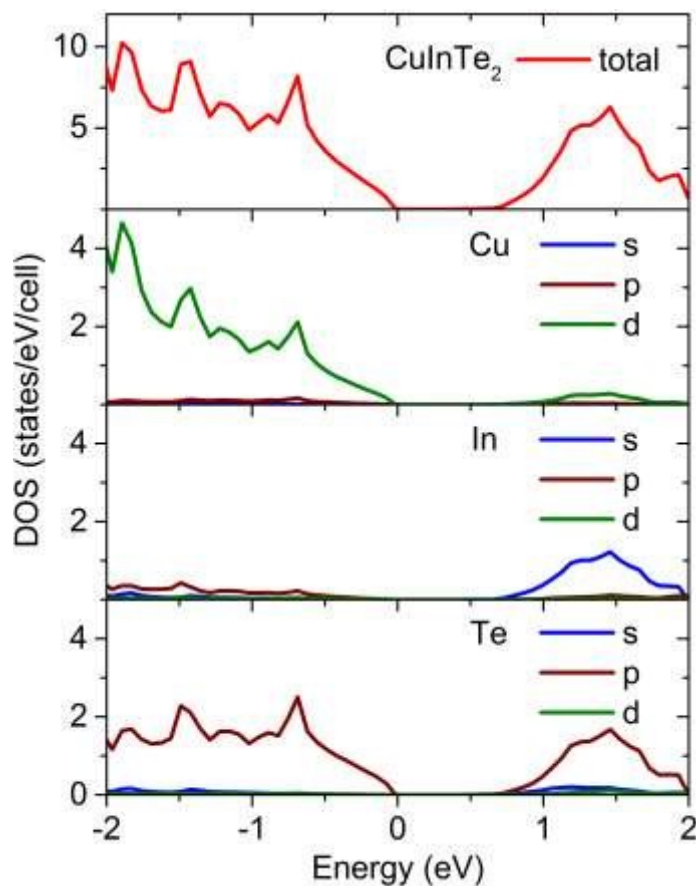
Figure 2. Total and atom-projected density of states of CuInTe$_2$.

We plotted the total and atom-projected density of states (DOS) of CuInTe$_2$ in Fig. 2. It can be seen from Fig. 2 that the energy states near the valence band edge primarily come from the hybridization of 3d orbitals of Cu atoms and 5p orbitals of Te atoms, which form a conducting pathway for charge carriers in the p-type semiconductors. The energy states near the conduction band edge are mainly due to the hybridization of the In 4s and Te 5p orbitals, which can provide a conducting pathway for charge carriers in the n-type semiconductors. The total DOS near the valence band edge is steeper while that near the conduction band edge is very flat at first then becomes steep with increasing energy, as in line with the band structures. It

can be expected that a steep slope of DOS near the band gap should lead to a high
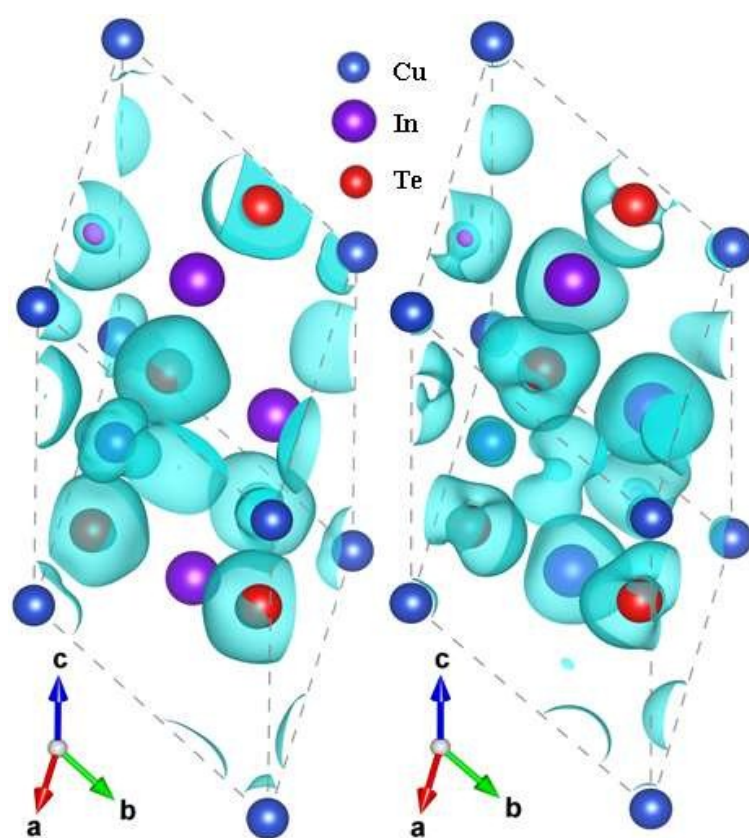
Seebeck coefficient.[24, 26, 27]

Figure 3. Partial charge density of CuInTe$_2$ for the bands near the Fermi level. The left panel

represents the upper parts of valence bands within a 2eV window below the VBM, with isosurface

value of 0.0025 e/bohr^3; the right panel represents the lower parts of conduction bands within a

2eV window above the CBM, with isosurface value of 0.0035 e/bohr^3.

To further identify the optimal doping sites, the partial charge densities for the

bands near the Fermi level are illustrated in Fig. 3. The left panel of Fig. 3 shows that

electrons are mostly distributed around the Cu and Te atoms and that around In atoms

is nearly invisible, which is in accordance with the atom-projected DOS. Thus,

p-doping at the In site will not substantially modify the electronic structures near the

edge of valence bands, which provides us a doping site to optimize the carrier

concentration to improve the thermoelectric figure of merit of CuInTe$_2$. The right

panel of Fig. 3 shows that charge density mainly distribute around In and Te atoms,

forming [In-Te-In] conducting network for electron transport. This illustrates that

n-doping (or substitution) at the Cu-site will only change the carrier concentrations

with little effects on the shape of the conduction band minimum (CBM).
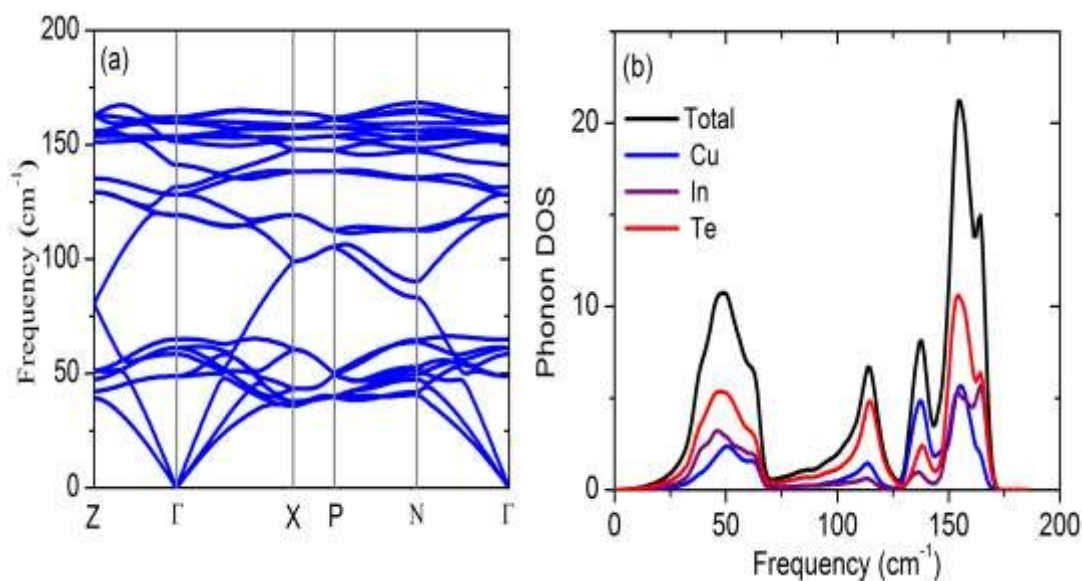
Figure 4. Phonon dispersion curves (a) and total density of states (b) for

CuInTe$_2$. The partial phonon DOS projected onto Cu, In and Te atoms are also shown.

The phonon-dispersion curves and the vibrational density of states for CuInTe$_2$

are shown in Fig. 4. Our calculated phonon frequencies are consistent with the

experimental data.[28] For example, the lowest optical phonon frequency (48.7 cm^{-1}) at

Γ-point is very close to the experimental value (48 cm^{-1}).[28] The optical phonon

modes exhibit weak dispersion, and these flat optical branches contribute negligibly to

heat transport because their group velocities are small.[29] As compared to optical

phonon modes, the low-frequency acoustic modes below 50 cm^{-1} are highly

dispersive and have larger group velocities. Therefore, these heat-carrying acoustic

modes will dominate the thermal transport properties in perfect bulk CuInTe$_2$. Fig. 4(a)

shows that some optical modes have very low frequencies around 50 cm^{-1} and are

mixed with the acoustic modes. These low lying optical phonon modes will induce

scattering due to their anharmonic coupling to the acoustic phonon modes, which can

effectively reduce the thermal conductivity of CuInTe$_2$.[30] It can be seen from Fig. 4(b) that the modes are mixed states composed of the Cu, In, and Te atoms in whole range of frequency and Te atoms have largest contribution to total phonon DOS except for a frequency range from 127 cm^{-1} to 147 cm^{-1}. Besides, either Cu, In, or Te lattice sites can be used as effective sites to introduce structural defects to induce additional phonon scattering with low-frequency acoustic modes and thus decrease the phonon thermal conductivity of CuInTe$_2$.
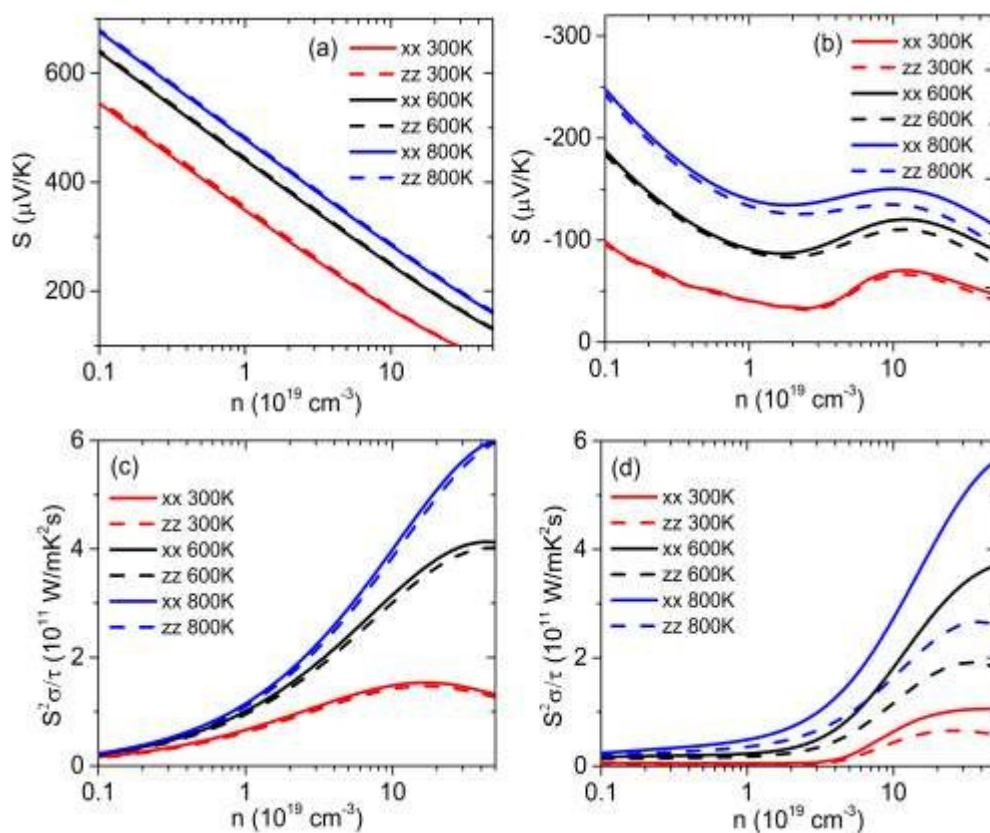

13

Figure 5. Anisotropic thermoelectric transport properties of CuInTe₂ as a function of carrier concentrations at different temperatures: p-type Seebeck coefficients (a), n-type Seebeck coefficients (b), p-type power factors $S^2\sigma/\tau$ (c), and n-type power factors $S^2\sigma/\tau$ (d). Here the xx and zz directions correspond to a-axis and c-axis, respectively.

We firstly calculated Seebeck coefficients of CuInTe₂ in different crystallographic directions. as a function of carrier concentrations at three different temperatures of 300, 600 and 800 K, as shown in Fig. 5(a) and (b). For p-type CuInTe₂, the presence of nearly degenerate valence bands near the Fermi level is responsible for this high Seebeck coefficient. For n-type case, Seebeck coefficients first decrease then increase with carrier concentration, which is due to the conduction-band dispersion near the Fermi level varying from steep to flat. At all temperatures and carrier concentrations, the Seebeck coefficient of p-type CuInTe₂ is larger than that of n-type one, which mainly originates from the fact that DOS near the edge of valence band is significantly steeper than that near the edge of conduction band. Additionally, we find that the Seebeck coefficient is isotropic for p-type CuInTe₂ and exhibits a little anisotropy for n-type one at higher carrier concentrations. From Fig. 5(a), it is found that the magnitude of S decreases with increasing n in the range of carrier concentrations. From Maxwell-Boltzmann approximation (when $E_F - E_v \gg k_B T$), one can derive an expression for S:[26, 31]

$$S = -\frac{k_B}{e}\ln\left(\frac{n}{N_v}\right) + \frac{k_B}{e}A_v \tag{7}$$

where N_v is the effective density of states near the valence band edge and A_v

14

represents a scattering factor. N_v can be expressed as

$$N_v = \int_{-\infty}^{E_v} g_v(\varepsilon) \exp\left[-(E_v - \varepsilon)/k_B T\right] d\varepsilon, \tag{8}$$

where $g_v(\varepsilon)$ is the density of states, E_v is the valence band edge. Eq. (7) directly reveals that for p-type doping the magnitude of S decreases with increasing n, as shown in Fig. 5(a). In analogy, one can obtain a similar equation and explain the linear dependence displayed in n-type case. It can be observed from Fig. 5(b) that the dependence of Seebeck coefficient on carrier concentration deviates from the linear behavior and appears a local minimum. This could be attributed to the multi-band effect, which indicates contributions of different bands to the Seebeck coefficient could have different signs and vary with temperature and doping concentration. We also evaluated the thermoelectric power factor $S^2\sigma/\tau$ of CuInTe$_2$ in different crystallographic directions as a function of carrier concentration at three different temperatures of 300, 600 and 800 K. While $S^2\sigma/\tau$ of p-type CuInTe$_2$ is nearly isotropic (Fig. 5(c)), there is considerable anisotropy in n-type one (Fig. 5(d)). Another key observation is that the optimized carrier concentration that maximizes $S^2\sigma/\tau$ depends on the temperature and as the temperature increases, higher carrier concentrations are required to maximize $S^2\sigma/\tau$.
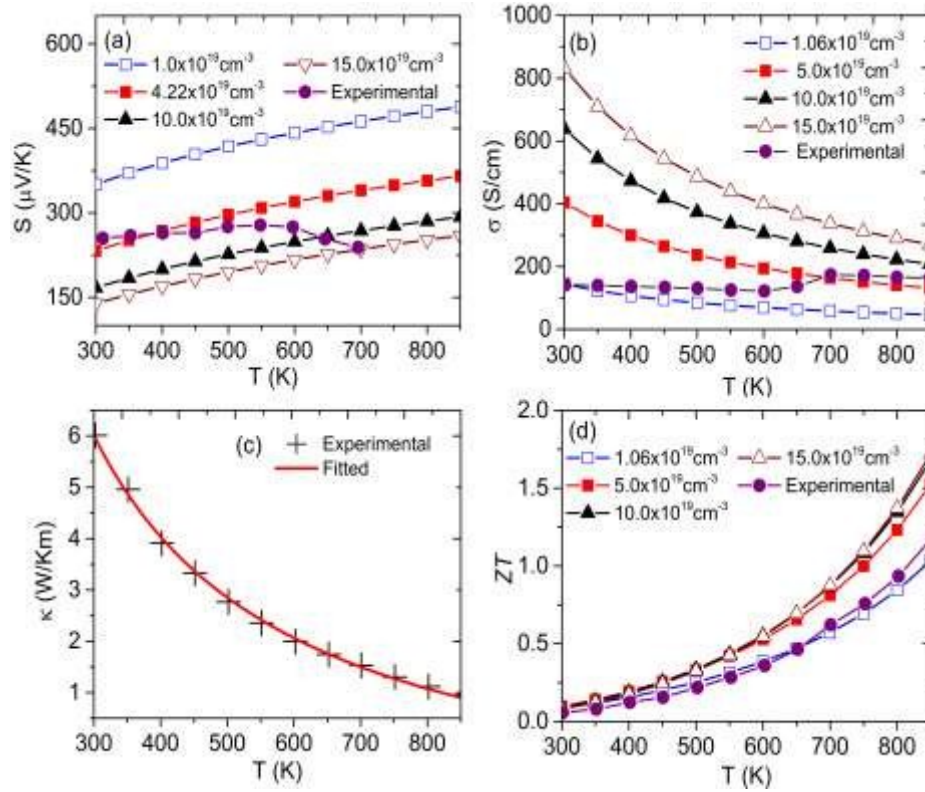
Figure 6. Seebeck coefficient (a), electrical conductivity (b), phonon thermal conductivity (c) and figure of merit (d) of p-type CuInTe$_2$ as a function of temperature at different carrier concentrations. The experimental data are plotted for comparison.

Fig. 6 shows the Seebeck coefficient (a), electrical conductivity (b), thermal conductivity (c) and figure of merit (d) of p-type CuInTe$_2$ as a function of temperature at different carrier concentrations. Fig. 6(a) shows the Seebeck coefficient increases with increasing temperature, which is mainly because the term, $\exp\left[-\left(E_v - \varepsilon\right)/k_B T\right]$ with $\varepsilon < E_v$ in Eq. (8) increases with rising temperature and then leads to an increasing N_v. The calculated Seebeck coefficients are in reasonable agreement with available experimental data with the carrier concentration value of 4.22×10^{19} cm^{-3} at 300 K.[12] There exists some discrepancy between theoretical and experimental data

16

and it becomes remarkable at higher temperature regime. This is most likely because

the carrier concentrations of measured CuInTe$_2$ samples vary with temperature due to

the thermal excitation. The behavior that Seebeck coefficients first rise then drop with

increasing temperature has been reported in previous experimental works.[32, 33] At high

temperatures electrons are thermally excited across the band gap and two different

types of carriers participate in transport, which is known as the bipolar effect. Then

the total Seebeck coefficient is given by[34]

$$S = \frac{\sigma_e S_e + \sigma_h S_h}{\sigma_e + \sigma_h} \tag{9}$$

where S_e and S_h are the Seebeck coefficient of electrons and holes, respectively;

σ_e and σ_h are the electrical conductivity of electrons and holes, respectively.

According to Eq. (9), the Seebeck coefficient will be significantly suppressed due to

electrons and holes having opposite charges (S_e and S_h have opposite signs). In our

calculations the carrier concentrations are instead kept fixed when the temperature

increases by tuning the chemical potential in the Fermi-Dirac distribution function.

We determined the charge carrier relaxation time empirically according to

conductivity measurements in the previously published paper.[11] Generally the

relaxation time τ depends on the temperature and carrier concentration, [11] and may

be expressed as follows:[35]

$$\tau = \lambda n^{-1/3} T^{-1} \tag{10}$$

where n is carrier concentration, T is temperature and λ is constant. Ruiheng

Liu and co-workers reported experimental electrical conductivity σ of 14431 S/m

for CuInTe$_2$ with the carrier concentration of 1.06×10^{19} cm^{-3} at 300 K.[11] By comparing

it with the calculated σ/τ, we yield τ is equal to 2.58×10^{-14} s at the same carrier concentration and temperature. Based on the obtained τ, one can determine λ and $\tau(n,T)$ as a function of carrier concentration and temperature. Fig. 6(b) shows the absolute value of electrical conductivity of CuInTe$_2$ obtained according to Eq. (10). Since the scattering rate increases with temperature, the electrical conductivity decreases with increasing temperature. When the temperature is lower than 650 K, the calculated results agree well with the experimental data.[11] For the same reason discussed above (thermal excitations), the theoretical data deviate from the experimental observations in the higher temperature regime as shown in Fig. 6(b).

In the higher temperature limit, phonon scattering dominates the lattice thermal conductivity. The phonon thermal conductivity κ_L generally obeys T^{-1} Umklapp phonon scattering behavior.[35] Here, we fitted the thermal conductivity of CuInTe$_2$ by adopting the formula $\kappa = a + b/T$. The fitted thermal conductivity κ is plotted in Fig. 6(c), which matches well with the experimental data. The calculated figure of merit ZT of p-type CuInTe$_2$ as a function of temperature is shown in Fig. 6(d). Theoretically, the ZT displays an increasing trend with temperature. The calculated values are higher than the experimental data at same carrier concentration (1.06×10^{19} cm^{-3}),[11] mainly originating from the fact that the calculated Seebeck coefficients are higher than the measured values (see Fig. 6(a)). Overall, CuInTe$_2$-based materials under the optimal level of doping are very promising for thermoelectric applications in the medium temperature range.
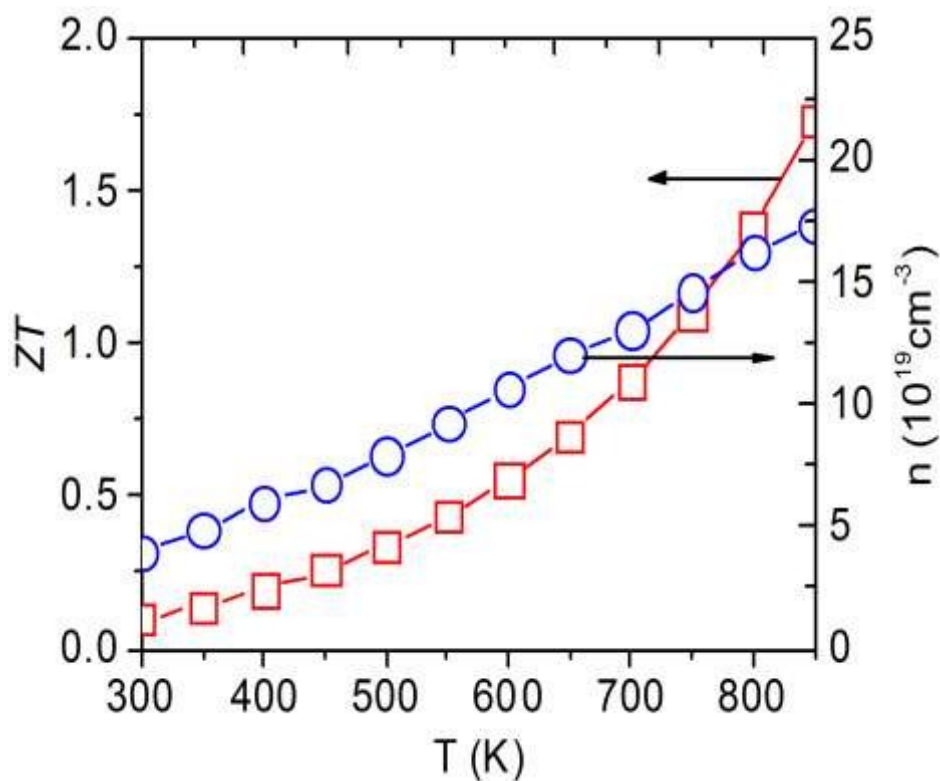
Figure 7. Optimized figure of merit of p-type $CuInTe_2$ and the corresponding carrier concentrations as a function of temperature.

The upper bound value for ZT and the corresponding carrier concentration as a function of temperature are shown in Fig. 7. Both optimized ZT and corresponding carrier concentration increase with the increasing temperature. The p-type $CuInTe_2$ can achieve the highest optimized ZT value of 1.72 at 850 K, which is fairly high and implies an energy-conversion performance comparable to that of commercially available thermoelectric materials. The corresponding optimized carrier concentration increases with temperature and change in the range from 5×10^{19} to 20×10^{19} cm^{-3}.

Physical Chemistry Chemical Physics Accepted Manuscript

Conclusions

In conclusion, we have performed density functional calculations on the CuInTe$_2$ system and analyzed its band structures, phonon and thermoelectric transport properties. From the analysis of DOS and partial charge density, it is found that there exists three-dimensional [–Cu–Te–Cu–] and [–In–Te–In–] conducting network to act as the channels for hole transport and electron transport, respectively. Moreover, In-site and Cu-site doping is suitable for tuning carrier concentrations without unduly damaging the hole and electron transport networks, respectively. Lattice-dynamics calculations indicate that introducing structural defects at Cu, In or Te sites may prove effective in reducing the lattice thermal conductivity, and the calculated phonon frequencies also agree with the experimental data. The p-type CuInTe$_2$ exhibits better thermoelectric properties as compared to the n-type one, which mainly originates from the steeper DOS resulting from nearly degenerate valence bands near the edge of valence band. The dependence of thermoelectric transport properties on the doping level and temperature was investigated in detail, which provides a guidance for future experiments to optimize *ZT* values of CuInTe$_2$. We predicted that p-type CuInTe$_2$ could exhibit high thermoelectric performance by optimizing hole-doped carrier concentrations and the corresponding optimized carrier concentration is in the range of 5×10^{19} cm^{-3} to 20×10^{19} cm^{-3}.

Acknowledgements

References

1.   K. Biswas, J. He, I. D. Blum, C.-I. Wu, T. P. Hogan, D. N. Seidman, V. P. Dravid and M. G. Kanatzidis, *Nature*, 2012, **489**, 414-418.

2.   M. S. Dresselhaus, G. Chen, M. Y. Tang, R. Yang, H. Lee, D. Wang, Z. Ren, J. P. Fleurial and P. Gogna, *Adv. Mater.*, 2007, **19**, 1043-1053.

3.   G. J. Snyder and E. S. Toberer, *Nat. Mater.*, 2008, **7**, 105-114.

4.   J. P. Heremans, V. Jovovic, E. S. Toberer, A. Saramat, K. Kurosaki, A. Charoenphakdee, S.

Yamanaka and G. J. Snyder, *Science*, 2008, **321**, 554-557.

5. J. P. Heremans, M. S. Dresselhaus, L. E. Bell and D. T. Morelli, *Nat. Nanotech.*, 2013, **8**, 471-473.

6. G. Zhou, L. Li and G. Li, *Appl. Phys. Lett.*, 2010, **97**, 3112.

7. X. Shi, J. Yang, J. R. Salvador, M. Chi, J. Y. Cho, H. Wang, S. Bai, J. Yang, W. Zhang and L. Chen, *J. Am. Chem. Soc.*, 2011, **133**, 7837-7846.

8. D. Wu, L.-D. Zhao, X. Tong, W. Li, L. Wu, Q. Tan, Y. Pei, L. Huang, J.-F. Li and Y. Zhu, *Energy Environ. Sci.*, 2015.

9. A. Majumdar, *Science*, 2004, **303**, 777-778.

10. Y. He, T. Day, T. Zhang, H. Liu, X. Shi, L. Chen and G. J. Snyder, *Adv. Mater.*, 2014, **26**, 3974-3978.

11. R. Liu, L. Xi, H. Liu, X. Shi, W. Zhang and L. Chen, *Chem. Commun.*, 2012, **48**, 3818-3820.

12. H. Chen, C. Yang, H. Liu, G. Zhang, D. Wan and F. Huang, *CrystEngComm*, 2013, **15**, 6648-6651.

13. J. Yang, S. Chen, Z. Du, X. Liu and J. Cui, *Dalton Trans.*, 2014, **43**, 15228-15236.

14. J. Yan, P. Gorai, B. Ortiz, S. Miller, S. A. Barnett, T. Mason, V. Stevanović and E. S. Toberer, *Energy Environ. Sci.*, 2015, **8**, 983-994.

15. G. Kresse and J. Hafner, *Phys. Rev. B*, 1993, **47**, 558.

16. G. Kresse and J. Furthmüller, *Comput. Mater. Sci.*, 1996, **6**, 15-50.

17. G. Kresse and J. Furthmüller, *Phys. Rev. B*, 1996, **54**, 11169.

18. J. P. Perdew, J. Chevary, S. Vosko, K. A. Jackson, M. R. Pederson, D. Singh and C. Fiolhais, *Phys. Rev. B*, 1992, **46**, 6671.

19. Y. Zhang, X. Yuan, X. Sun, B.-C. Shih, P. Zhang and W. Zhang, *Phys. Rev. B*, 2011, **84**, 075127.

20. A. Togo, F. Oba and I. Tanaka, *Phys. Rev. B*, 2008, **78**, 134106.

21. G. K. Madsen and D. J. Singh, *Comput.Phys.Commun.*, 2006, **175**, 67-71.

22. N. W. Ashcroft and N. D. Mermin, *Solid State Physics*, Holt, Rinehart and Winston, New York, 1976.

23. D. Parker and D. J. Singh, *Phys. Rev. B*, 2012, **85**, 125209.

24. A. F. May, D. J. Singh and G. J. Snyder, *Phys. Rev. B*, 2009, **79**, 153101.

25. L. Xi, Y. Zhang, X. Shi, J. Yang, X. Shi, L. Chen, W. Zhang, J. Yang and D. J. Singh, *Phys. Rev. B*, 2012, **86**, 155201.

26. G. Zhou and D. Wang, *Sci. Rep.*, 2015, **5**, 8099.

27. G. Mahan and J. Sofo, *Proc. Natl. Acad. Sci.USA*, 1996, **93**, 7436-7439.

28. C. Rincón, S. Wasim, G. Marın, E. Hernández, J. Delgado and J. Galibert, *J. Appl. Phys*, 2000, **88**, 3439-3444.

29. K. Biswas and C. W. Myles, *Phys. Rev. B*, 2007, **75**, 245205.

30. G. Lan, B. Ouyang and J. Song, *Acta Mater.*, 2015, **91**, 304-317.

31. G. Zhou, L. Li and G. Li, *J. Appl. Phys.*, 2011, **109**, 114311.

32. D. Kraemer, J. Sui, K. McEnaney, H. Zhao, Q. Jie, Z. Ren and G. Chen, *Energy Environ. Sci.*, 2015, **8**, 1299-1308.

33. L.-D. Zhao, S.-H. Lo, Y. Zhang, H. Sun, G. Tan, C. Uher, C. Wolverton, V. P. Dravid and M. G. Kanatzidis, *Nature*, 2014, **508**, 373-377.

34. D. B. Luo, Y. X. Wang, Y. L. Yan, G. Yang and J. M. Yang, *J. Mater. Chem. A*, 2014, **2**,

15159-15167.

35.   K. P. Ong, D. J. Singh and P. Wu, *Phys. Rev. B*, 2011, **83**, 115110.